Research Article Vol. 13, No. 12 / 1 Dec 2023 / Optical Materials Express 3715
Optical Materials EXPRESS

Design of cost-effective environment-responsive nanoacoustic devices based on mesoporous thin films

EDSON R. CARDOZO DE OLIVEIRA,[1] PRISCILA VENSAUS,[2] GALO J. A. A. SOLER-ILLIA,[2] AND NORBERTO DANIEL LANZILLOTTI-KIMURA[1,*]

[1] *Université Paris-Saclay, CNRS, Centre de Nanosciences et de Nanotechnologies, 91120 Palaiseau, France*
[2] *Instituto de Nanosistemas, Escuela de Bio y Nanotecnologías, Universidad Nacional de San Martín-CONICET, Buenos Aires, Argentina*
[*] *daniel.kimura@c2n.upsaclay.fr*

Abstract: Gigahertz acoustic resonators have the potential to advance data processing and quantum communication. However, they are expensive and lack responsiveness to external stimuli, limiting their use in sensing applications. In contrast, low-cost nanoscale mesoporous materials, known for their high surface-to-volume ratio, have shown promise in various applications. We recently demonstrated that mesoporous silicon dioxide (SiO_2) and titanium dioxide (TiO_2) thin layers can support coherent acoustic modes in the 5 to 100 GHz range. In this study, we propose a new method for designing tunable acoustic resonators using mesoporous thin films on acoustic distributed Bragg reflectors. By simulating the infiltration of the pores with water, we show that the material's properties could be altered and achieve tunability in the acoustic resonances. We present four device designs and use simulations to predict resonators with Q-factors up to 1500. We also observe that the resonant frequency and intensity show a linear response to water infiltrated in the mesopores, with a tunability of up to 60%. Our platform offers a unique opportunity to design cost-effective nanoacoustic sensing and reconfigurable optoacoustic nanodevices.

1. Introduction

The potential of nanophononics – the engineering and manipulation of acoustic phonons at the nanoscale –, [1–7] has been established within various technological applications, including heat management, data processing, and quantum technologies. The field explores how the interaction between GHz acoustic phonons and other excitations, dependent on the position of the atoms in a lattice, can be leveraged to engineer novel and more efficient devices in phonon-based optoelectronics, [8–12] photonics, [4,13–18] plasmonics, [19–22], polaritonics, [23–25] and other related areas. To precisely tailor the phononic response and produce high-quality devices, expensive techniques such as molecular beam epitaxy and electron beam lithography are typically employed [5,21,22,26]. However, there is a growing demand for cost-effective and reliable fabrication processes in engineering artificial materials for high-frequency acoustic applications. One promising solution is using nanoscale mesoporous materials, which possess a high surface-to-volume ratio and tailorable mesopores [27–30]. These materials allow for chemical functionalization, [31,32] have versatile optical applications, [33,34] and offer a phononic response within the GHz range [35–39].

In recent works, we reported the successful development of mesoporous silicon dioxide (SiO_2) and titanium dioxide (TiO_2) thin layers capable of supporting coherent acoustic modes spanning from 5 to 100 GHz, with Q-factors ranging from 5 to 17 [36,37]. These materials were obtained through simple and cost-effective soft chemical methods (sol-gel, self-assembly, dip- or

#504926 https://doi.org/10.1364/OME.504926
Journal © 2023 Received 6 Sep 2023; revised 12 Nov 2023; accepted 14 Nov 2023; published 30 Nov 2023

Optical Materials EXPRESS

spin-coating processes), which reproducibly generate optical quality films or multilayers with complex architectures and tunable properties [28,32,40,41]. Building upon this progress, we theoretically investigate a platform for engineering complex mesoporous systems specifically designed to support targeted high-frequency acoustic phonon modes that change upon infiltration of molecules in the mesopores, thus rendering these systems responsive to environment and optimizing their performance for sensing or actuating applications. Our proposed structures consist of a mesoporous surface cavity placed atop an acoustic distributed Bragg reflector (DBR), enabling the confinement of phonons at 100 GHz. By incorporating environmental molecules into the pores and manipulating the elastic properties of the metamaterial, the mesoporous layer could potentially serve as the active element for optoacoustic responsive applications that include sensors, transducers or actuators [35].

Our simulation results demonstrate the presence of robust coherent phonon signals at the desired frequency, offering the potential for achieving high Q-factors. In addition, we demonstrate that infiltration of a second component in the mesopores (e.g., a liquid, polymer or biomolecule) leads to appreciable changes in frequency location and shape. This significant advancements pave the way for a promising platform in responsive and reconfigurable optoacoustic nanodevices, all made possible through the utilization of soft and cost-effective fabrication methods.

2. Methodology

In a pump-probe coherent phonon generation experiment, standard technique in nanophononics, a strong laser pulse, namely the pump, interacts with the structure, triggering the phononic dynamics in the system. The modulation of the material refractive index due to these vibrations, i.e., the photoelastic interaction, takes place. Finally, a delayed probe reaching the structure measures transient reflectivity changes due to the presence of coherent acoustic phonons [42,43]. In this work, we simulate the generation and detection spectra of coherent acoustic phonons in such an experiment and test different sample designs. This is done by implementing the photoelastic model using the standard transfer matrix method for acoustic and optical fields [13,44]. The theoretical approach employed here allows us to investigate multilayered structures with contrasting acoustic and optical impedances and test different parametrizations [13]. The material parameters used in the simulations are presented in Table 1.

Table 1. Optical and elastic properties of the studied materials for the numerical simulation.

Material	Index of refraction	Speed of sound (m/s)	Density (g/cm^3)
dSiO_2	1.45	5750	2.2
dTiO_2	2.56	6700	2.9
dry mSiO_2[a]	1.26	3587	1.32
Nickel	2.218+4.893i	5580	8.908
Air	1.0003	343	1.28x10^{-3}
Water	1.33	1480	0.997
Glass	1.538	5750	2.2

[a]Dry mesoporous SiO_2, considering a porosity of 40%. Refer to section 2.1 for details on the speed of sound and density at different humidities.

We assume a white phonon spectrum propagating from the substrate towards the surface and compute the normalized stationary solutions for each phonon frequency. This allows us to calculate the acoustic phonon transmission spectrum and determine the frequency-dependent acoustic field distribution along the structure. Analogously, the incident laser electric field profile can be calculated by considering Maxwell's equations for electromagnetic waves [45]. We assume standard boundary conditions, and a monochromatic laser to simplify the formulation.

Optical Materials EXPRESS

Finally, we determine the acoustic phonon generation spectrum ($G(\omega)$) with an overlap integral of the incident pump's electric field ($E(\nu, z)$), the strain field ($\eta(\omega, z)$), i.e., the derivative of the acoustic displacement, and the material-dependent transduction constant ($k(z)$), as follows:

$$G(\omega) = \int k(z)\eta(\omega, z)|E(\nu, z)|^2 dz, \tag{1}$$

where ω and ν correspond to the acoustic and optical frequencies, respectively. The coherent phonon detection spectrum, which can be related to the modulation of the probe reflectivity ($\Delta R(\omega)$), is then calculated by considering the photoelastic interaction in the material. This is done by calculating an overlap integral similar to Eq. (1), but taking into account the generation spectrum and the probe's complex electric field, in the form:

$$\Delta R(\omega) = \int G(\omega)k(z)\eta(\omega, z)E(\nu, z)^2 dz \tag{2}$$

Additionally, we can determine the surface displacement by multiplying the phonon generation spectrum with the transmission spectrum:

$$d(\omega) = G(\omega)T(\omega) \tag{3}$$

Experimentally, the surface displacement can be measured by implementing an interferometer in the pump-probe setup, which involves sensitive alignment procedures [46]. While it is easier to probe changes in reflectivity, the analysis of surface displacement becomes necessary depending on the specific sample under investigation [36,37].

It is worth noting that our analysis assumed that the optical absorption and coherent phonon generation are limited to the nickel transducer layer.

2.1. Mesoporous material parameters as a function of water content

In order to study the dependence of the acoustic phonon detection spectrum on changes in the relative humidity, we calculate weighted averages of the mesoporous mass density (ρ) and speed of sound (v), considering the dense SiO_2 matrix, water and air, according to

$$X = X_{\text{solid}}\,(1 - p) + [X_{\text{air}}\,(1 - h) + X_{\text{water}}h]\,p, \tag{4}$$

where $X = v$ or ρ, and p and h correspond to the porosity and water content. In addition, the refractive index (n) is calculated according to the Bruggeman approximation for a mixture of the three dielectric media states [47]. The new optical and elastic parameters are then used as inputs to calculate the wave propagation in the multilayered structures for the electromagnetic field and sound using the transfer matrix method. We perform the simulation for all the acoustic resonators with a constant porosity $p = 40$ %.

3. Design of mesoporous surface acoustic resonators

Mesoporous materials are known for their ability to adsorb chemical compounds into the mesopores [48,49]. This leads to effective functionalization of the materials, that can be sensitive to different external stimuli. In the context of nanoacoustics, the chemical infiltration modifies the overall optical and elastic properties of the material, such as refractive index (n), mass density (ρ), and speed of sound (v). The simplest acoustic resonator can be engineered by embedding a mesoporous thin film (MTF) between two layers with contrasting acoustic impedance $Z = \rho v$. Depending on the relative impedances of the layers, the resonator will support frequency modes

Optical Materials EXPRESS

according to either

$$f_n = \frac{Nv}{2d} \tag{5a}$$

or

$$f_n = \frac{(2N-1)v}{4d}, \tag{5b}$$

where d and $N = 1, 2, 3\cdots$ are associated with the mesoporous thickness and mode order, respectively. Here, the acoustic resonances in the mesoporous materials can be determined with the Eq. (5a) The acoustic impedance mismatch between the layers, given by the contrast in mass density and speed of sound of the involved materials, can account for enhanced transmission or reflection of the sound waves at the interfaces. Therefore, chemical infiltration into the mesopores can significantly change the resonance frequency – by changing the v –, and the Q-factor of the confined modes – by changing v and ρ. A simple approach could be to submit the device to different relative humidity (RH) conditions, which could be extended for sensing different gases.

In fact, phonon confinement in mesoporous thin films based on SiO_2 and TiO_2 has been recently reported in pump-probe experiments [36,37]. In such works the mesoporous layer was embedded between a glass substrate and a nickel thin-film that acts as the acousto-optical transducer. Two major constraints arise from this design: the mesoporous thin film is covered by other layers, which prevents efficient adsorption into the mesopores; and the leakage of the acoustic waves towards the substrate reduces the Q-factor of the resonator.

To overcome these limitations we propose a device design composed of the MTF as the outermost layer in the structure, followed by the nickel transducer and an acoustic distributed Bragg reflector (DBR) based on dense SiO_2/TiO_2 on top of a glass substrate. Acoustic DBRs based on semiconductors have been used to develop Fabry-Perot-like resonators for high-frequency acoustic phonons in multilayered structures [14,50–55]. On one hand, in our devices, the acoustic DBR designed at a frequency $f = 100$ GHz has an acoustic stop-band that reflects the frequency components within this band, as shown in Figure 1. On the other hand, GHz acoustic phonons are entirely reflected at the mesoporous/air interface, as they do not propagate into the air. In addition, since the mesoporous SiO_2 is a transparent material for the studied optical range (near infrared), the phonon generation takes place in the nickel layer upon light absorption, mainly via photoinduced thermoelasticity [43]. With that, by properly engineering the thicknesses of the layers, it is possible to tune the DBR stop-band and develop a surface acoustic cavity confining phonons at the mesoporous layer. This has already been demonstrated with oxide DBRs based on $BaTiO_3$/$SrTiO_3$, where a Ni thin film is deposited on top of the DBR to generate and detect high-frequency acoustic phonons located at the metal-oxide interface [56].

The acoustic resonators (ARs) proposed here are formed by four different elements. We engineer and numerically investigate four distinct variations of ARs, shown in Figs. 2(a-d). These variations involve different combinations of layers. Our objective is to identify the optimal configuration that exhibits the strongest correlation between acoustic resonance and the infiltration of liquids into the mesopores. The devices are formed by a glass substrate, followed by a 3-periods-DBR of TiO_2/SiO_2 ($\lambda/4$, $\lambda/4$) designed to operate at 100 GHz, where λ corresponds to the acoustic wavelength at the design frequency. The structures are named AR1, 2, 3 and 4. ARs 1-3 have an extra $\lambda/4$ TiO_2 layer before the $\lambda/4$ Ni transducer. After the nickel, the four structures have a combination of zero, one, or two $\lambda/4$ dense layers before finalizing with the mesoporous layer. With these configurations, the mesoporous thickness leading to phonon confinement at 100 GHz is $\lambda/2$ for AR1, AR3, and AR4, and $\lambda/4$ for AR2. The layer thicknesses of SiO_2, TiO_2, Ni, mesoporous ($\lambda/2$) and mesoporous ($\lambda/4$) are 14.4 nm, 16.8 nm, 14.0 nm, 17.9 nm and 9.0 nm, respectively. We also consider acoustic losses in the mesoporous layer with an effective phonon decay length of 90 nm [36].

Figure 2(e) displays the simulated phononic spectra of all the structures, considering the modulation of the refractive index of the Nickel layer, with a pronounced acoustic mode at 100

Optical Materials EXPRESS

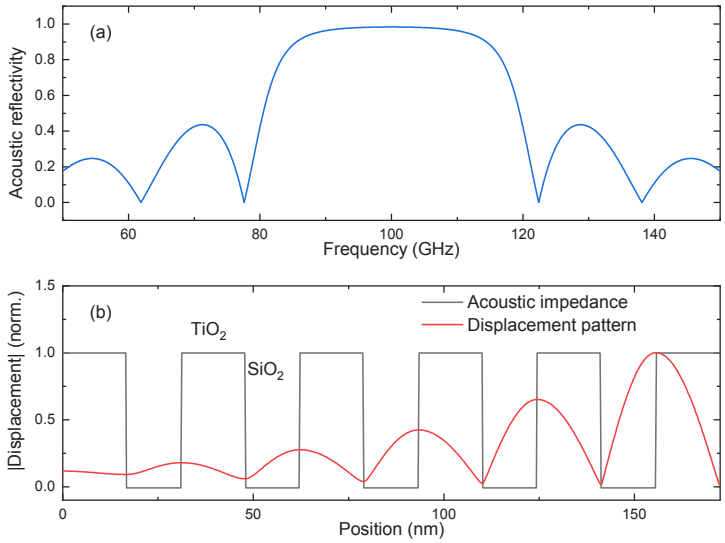

Fig. 1. (a) Response of the acoustic DBR formed by dense SiO_2/TiO_2 layers, showing a stop band centered at 100 GHz. (b) The acoustic displacement pattern at 100 GHz (red) and the acoustic impedance (black) along the structure. The SiO_2 and TiO_2 layers have thicknesses of 14.4 nm and 16.8 nm, respectively

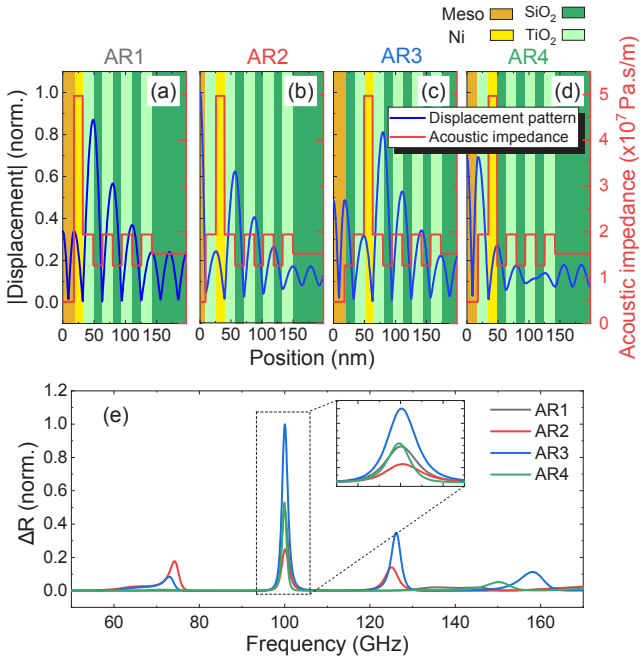

Fig. 2. (a-d) Normalized displacement pattern (blue) and acoustic impedance (red) of the surface cavity structures AR1-4. The layers of mesoporous, nickel, SiO_2 and TiO_2 are represented by the colors orange, yellow, blue, and green, respectively. (e) Reflectivity spectra for the structures presented in panels (a-d). The inset represents an enlargement of the peak at 100 GHz.

Optical Materials EXPRESS

GHz. This result supports the use of a reflectometric experimental setup for detecting the acoustic resonances in the mesoporous layer. The acoustic resonance detection performed by the Ni layer indicates that its proximity to the mesoporous layer is not a critical requirement. The peaks at 75 GHz and 125 GHz indicate a stop-band spanning over ~50 GHz. The acoustic resonance in AR2 has the weakest response and is the strongest in AR3. To investigate the region in which the phonons are confined in the structures, the displacement pattern at 100 GHz is plotted, overlapped with the device profiles (blue curves of Figs. 2(a-d)), the maximum displacement indicates the region of phonon confinement. In such analysis, it is revealed that maximum displacement in AR1 and AR3 is at the last period of the acoustic DBR. On the other hand, AR2 and AR4 evidence phonon confinement at the mesoporous layer.

Usually, the fabrication of multilayered structures is susceptible to thickness fluctuations. When engineering acoustic resonators, the precise definition of the layer thicknesses is essential, and the thickness variation might compromise the phonon confinement. Notwithstanding, we study the photoelastic interaction as a function of the mesoporous layer thickness, in terms of phonon wavelength λ, ranging from $\lambda/4$ to λ, and the results are presented in Figure 3.

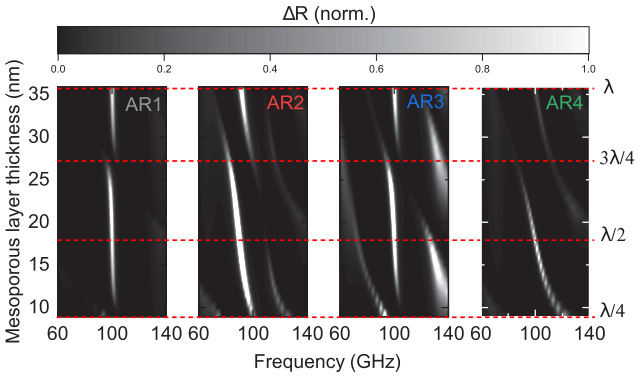

Fig. 3. Simulated coherent phonon generation-detection spectra as a function of the mesoporous layer thickness and frequency for AR1, AR2, AR3, and AR4. Horizontal dashed lines represent the key layer thicknesses in steps of a quarter of the phonon wavelength. Vertical dashed lines are guides to the design frequency of 100 GHz.

The mesoporous thicknesses for which the resonators exhibit the mode frequency at 100 GHz are $\lambda/2$ for AR1, AR3 and AR4, and $\lambda/4$ for AR2, in agreement with the designed structures. Furthermore, we can identify how sensitive the acoustic resonances are with the mesoporous thickness. By changing the layer thickness from $\lambda/4$ to $3\lambda/4$, the acoustic resonances of AR2 and AR4 span over $\sim$ 20 and $\sim$ 30 GHz, respectively. Conversely, AR1 and AR3 have minimum dependence on the mesoporous thickness, as the phonon confinement region is located between the Ni and the DBR. It is worth noting that the modes within the stop band persist, even if the resonance deviates from the specified 100 GHz.

4. Optimization of the devices

To determine the optimal responsivity of the proposed devices, we simulated the photoelastic interaction of structures with a different number of the dense SiO_2/TiO_2 bilayers composing the DBR, ranging from 2 to 10 periods, for the 4 structures. Afterward, the mode at f = 100 GHz in the full pump-probe simulation is fitted with a Lorentzian function, and both the integrated intensity and full width at half maximum (FWHM) are extracted. The results are shown in Figure 4.

Optical Materials EXPRESS

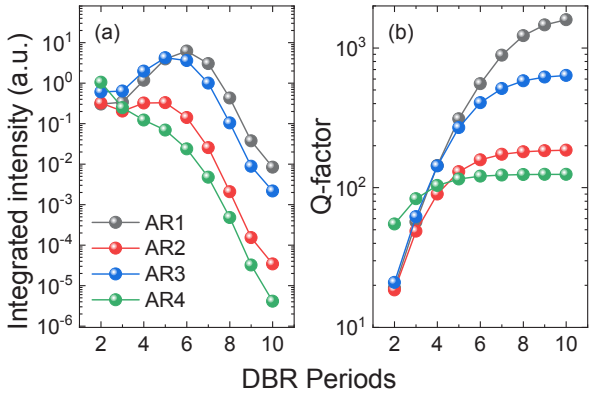

Fig. 4. (a) Integrated intensity and (b) quality factor of the acoustic mode at 100 GHz as a function of the number of DBR periods for the four proposed resonators.

The integrated intensity (Fig. 4(a)) is strongly dependent on the number of DBR periods, for all the ARs, changing up to five orders of magnitude over the calculated range. Maximum intensity is observed at 6 periods for AR1 and 5 periods for AR2 and AR3, and AR4 displays the maximum value at 2 periods. The quality factor (Q-factor), shown in Fig. 4(b), is calculated by the ratio between the mode frequency (100 GHz) and the extracted FWHM. All the resonators present an increase of the Q-factor as the number of DBR periods increases, as expected, showing a tendency for stabilization at higher periods. At 10 periods, the highest Q-factor, of ~1500, is for AR1, followed by AR3 (~630), AR2 (~180) and AR4 (~120).

5. Performance of the devices

Finally, we investigate the performance of the acoustic resonators over liquid infiltration into the nanopores. It is still unclear how acoustic resonators in the GHz range respond to the density and speed of sound changes in the MTF under liquid infiltration [36,37]. High-frequency coherent acoustic phonons are unable to penetrate into bulk liquids or gases; therefore, in principle they should remain entirely on the solid matrix without penetrating into the nanopores, and no response would be perceived. However, studies indicate that in mesoporous materials, liquids, such as water, strongly interact with the inorganic surface, which leads to a local organization, which is dependent of the mesopore diameter; this organized solvent can behave as a semi-condensed phase [57–59]. This allows high-frequency phonon penetration, leading to a change in the effective density, as well as in the speed of sound. The pore-load modulus, a quantity associated with the pressure inside the pores under liquid infiltration, has also been studied in silicon mesoporous membranes as a function of the material porosity [60]. Elucidating such effects is out of the scope of this work. Hereupon, in order to verify the effect of density and speed of sound change in the material, we consider weighted averages between the solid matrix, air, and water inside the pores, as described in section II.b, while keeping the other parameters (such as mesoporous layer thickness) constant. We perform the simulations for all the acoustic resonators varying the water loading in the mesopores between 0 and 100 %, in which the reference 100 GHz mode is calculated at 0 % water loading. By fitting a Lorentzian function on the acoustic resonance, we extract and analyze the frequency position, FHWM, and normalized intensity variation. The results for each of the peak properties are respectively depicted in Figs. 5(a), (b), and (c).

The water adsorption on the mesoporous layer influences the three peak parameters. All the resonators undergo a blueshift in frequency at higher water loading (Figs. 5(a)), which is related to the increase in the speed of sound. As the sound speed in the water is higher, the weighted

Optical Materials EXPRESS

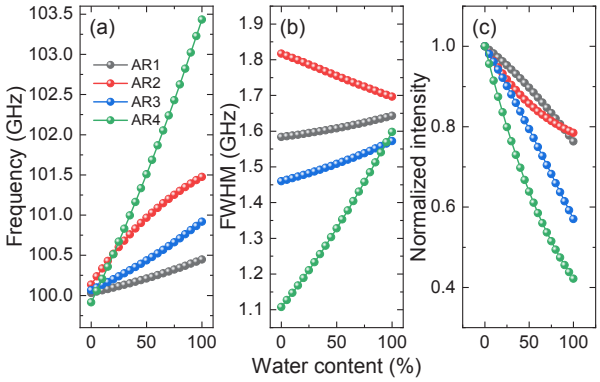

Fig. 5. (a) Frequency shift, (b) FWHM, and (c) normalized intensity of the mode at 100 GHz as a function of water content inside the pores for the four proposed structures.

average increases, and the resonator confines higher frequencies at the same region. It is worth noticing that AR1 is the least sensitive, with a frequency shift $\Delta f \sim 0.5$ GHz from 0 to 100 % RH, whereas AR4 is the most sensitive ($\Delta f \sim 3.5$ GHz). This can be justified by the fact that the confined mode of AR1 is not at the mesoporous layer, whereas AR4 displays clear confinement at this layer, as seen in Figs. 2(a) and (d). The highest sensitivity for AR4 and lowest for AR1 is also true for the analysis of FWHM. The linewidth of the resonance broadens for the resonators AR1, AR3, and AR4, whereas it narrows for AR2, as shown in Fig. 5(b). Liquid infiltration into the mesopores also leads to a decrease in the integrated intensity of the peak at 100 GHz for all the resonators (Fig. 5(c)), which reach values of $\sim$ 0.76, $\sim$ 0.78, $\sim$ 0.57, and $\sim$ 0.42 compared to the maximum intensity at 0 % RH, for each of the resonators AR1, AR2, AR3, AR4, respectively. This reduction in intensity comes from the fact that the mesoporous acoustic impedance increases under liquid infiltration, leading to a less efficient coupling of the acoustic waves to the transducer.

From Figure 5, we can conclude that for increasing quantities of water condensed within the mesopores, monotonous, nearly linear dependences of the signal positions and intensities are obtained, which is an essential aspect of the calibration and scaling of environment-sensitive devices. The design of AR4 is considered to provide the best sensitivity. Despite the observed differences, the four structures proposed here are potential candidates for sensing or acousto-optical switching applications. Further experimental efforts should explore this potential in detail. Additionally, the scope of the study could be expanded to include other systems, such as the detection of different vapors or liquids, even biomolecules, with distinct densities and sound velocities, which would likely yield varied yet distinguishable responses.

In addition to these changes in signal location and features, we could exploit a remarkable feature of mesoporous materials, such as the fact that vapors can condense in the mesopores in a narrow vapor pressure window, leading to a sudden and significant adsorption that changes the film properties. This characteristic was exploited to build optical vapor sensors based in photonic crystals (see e.g. [32] and [40]).

In order to link the water vapor pressure with the water pore filling, we resorted to water isotherms to rescale the pore filling with the corresponding equilibrium water vapor pressure. Figure 6(a) shows experimental water adsorption-desorption isotherms measured by environmental ellipsometric porosimetry [57] on two mesoporous thin films with pore volume around 40 % and presenting 2.2 nm and 7.8 nm pore diameter. Experimental values were extracted from previous work in mesoporous silica thin films [61]. The well-known features of water adsorption in mesoporous materials are observed: in a first stage, water adsorbs gradually in the mesopores along

Optical Materials EXPRESS

an increase in partial pressure (P/P_0). After a given critical P/P_0 value, capillary condensation takes place, and pores get filled with water. For higher vapor pressures, the film remains saturated in water; the desorption curve may present hysteresis. This behavior permits to imagine switchable behavior near the critical P/P_0 values. Figures 6(b) and 6(c) show the effect of the water vapor equilibrium in the resonant mode frequencies and intensities depending on the water partial pressure P/P_0, respectively. Similar features are observed that demonstrate that the responsivity can be translated to the acoustic phenomenon. These representations clearly demonstrate the potential of mesoporous thin films as optoacoustic devices responsive to external solicitations (in this case, water vapor pressure).

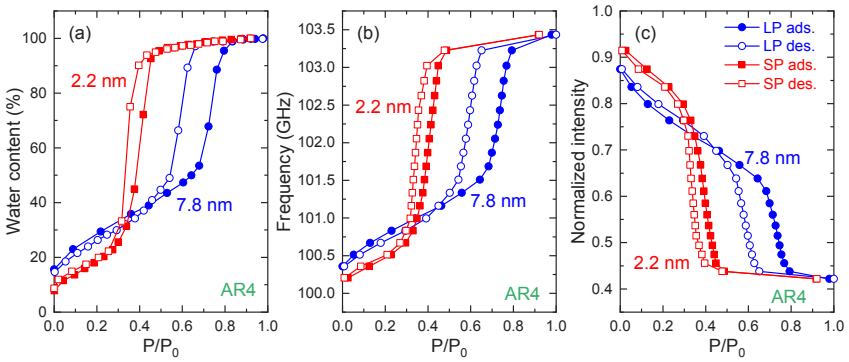

Fig. 6. (a) Water adsorption-desorption isotherm (adapted from [61]), (b) frequency shift, and (c) normalized intensity of the mode as a function of vapor pressure for the acoustic resonator AR4, considering mesoporous SiO_2 with average pore size distributions of 7.8 nm (blue) and 2.2 nm (red). LP and SP stand for large pores and small pores, respectively. Closed (open) symbols represent adsorption (desorption) processes.

The observed variation of signal location and shape changes upon water adsorption and/or capillary condensation can be advantageously used to fabricate optoacoustic devices responsive to the environment, with potential application in sensors, optoacoustic switches, environment-responsive waveguides or remote actuators. Solvent infiltration in mesoporous thin films can be exploited in any of the three regions discussed above (i.e., the gradual increase at low vapor pressures, the sharp changes in a narrow vapor pressure window corresponding to capillary condensation, the saturation). This has been particularly well studied in the case of water, which is a standard proof of concept for optical responsivity of films exposed to vapors [32,57]. The water adsorption properties and the critical responsivity of these films can be in principle finely tuned, as these features depend on controllable film parameters such as pore diameter, molecule content, or surface nature. The model can be easily extended to other liquids or molecules, just by taking into account the adequate elastic properties. Therefore, this work could open the path to the design of possible vapor-responsive optoacoustic systems that can be readily integrated with electronic or magnetic platforms.

6. Conclusion

We have introduced a new design for optoacoustic sensing devices featuring mesoporous thin film as the active component. By infiltrating the layer with liquid, the elastic properties of the thin film are gradually modified. As a result, an acoustic resonator employing these materials experiences an overall alteration of its resonance characteristics. We theoretically demonstrated the promising potential of these devices for environmental sensing. They can exhibit high-quality factors of up to 1500, a nearly linear response of peak parameters to changes in humidity, and a significant peak intensity variation of up to 60 %. The small size of the resonator and the

Optical Materials EXPRESS

short wavelength of GHz phonons offer a notable advantage over other sensors, as they enable significantly faster responsiveness. This means that a smaller volume of liquid infiltration is needed to achieve effective sensing. In principle, the unique characteristics and tunability of MTFs (i.e., controllable adsorption and capillary condensation, tunability) open new ways to create environment-responsive thin films through tunable phonon confinement, leading to low-cost nano-sensors, optoacoustic responsive guides or externally triggerable actuators. However, the requirement for all-optical experiments to investigate high-frequency acoustic phonons remains a significant roadblock for practical applications. This challenge could potentially be overcome by combining electrically contacted bulk acoustic wave resonators for efficient transduction [55,62]. Nevertheless, our findings shed light on a novel framework for nanoacoustic sensing and adaptable devices, utilizing cost-effective fabrication techniques.

Funding. ECOS-Sud Program (PA19N03); HORIZON EUROPE European Research Council (101045089); Agencia Nacional de Promoción de la Investigación, el Desarrollo Tecnológico y la Innovación (PICT 2017-4651, PICT 2020-03130, PICT-2018-04236).

Disclosures. The authors declare no conflicts of interest.

Data availability. Data underlying the results presented in this paper are not publicly available at this time but may be obtained from the authors upon reasonable request.

References

1. Priya, E. R. Cardozo de Oliveira, and N. D. Lanzillotti-Kimura, "Perspectives on high-frequency nanomechanics, nanoacoustics, and nanophononics," Appl. Phys. Lett. **122**(14), 140501 (2023).
2. A. A. Balandin, "Nanophononics: Phonon Engineering in Nanostructures and Nanodevices," J. Nanosci. Nanotech. **5**(7), 1015–1022 (2005).
3. S. Volz, J. Ordonez-Miranda, M. P. Andrey Shchepetov, *et al.*, "Nanophononics: State of the art and perspectives," Eur. Phys. J. B **89**(1), 15 (2016).
4. M. Trigo, A. Bruchhausen, A. Fainstein, *et al.*, "Confinement of Acoustical Vibrations in a Semiconductor Planar Phonon Cavity," Phys. Rev. Lett. **89**(22), 227402 (2002).
5. S. Anguiano, A. E. Bruchhausen, B. Jusserand, *et al.*, "Micropillar Resonators for Optomechanics in the Extremely High 19–95-GHz Frequency Range," Phys. Rev. Lett. **118**(26), 263901 (2017).
6. N. D. Lanzillotti-Kimura, A. Fainstein, A. Lemaître, *et al.*, "Nanowave devices for terahertz acoustic phonons," Appl. Phys. Lett. **88**(8), 083113 (2006).
7. N. D. Lanzillotti-Kimura, A. Fainstein, B. Jusserand, *et al.*, "Acoustic phonon nanowave devices based on aperiodic multilayers: Experiments and theory," Phys. Rev. B **76**(17), 174301 (2007).
8. B. Stiller, M. Merklein, C. Wolff, *et al.*, "Coherently refreshing hypersonic phonons for light storage," Optica **7**(5), 492 (2020).
9. P. Dainese, P. S. J. Russell, N. Joly, *et al.*, "Stimulated Brillouin scattering from multi-GHz-guided acoustic phonons in nanostructured photonic crystal fibres," Nat. Phys. **2**(6), 388–392 (2006).
10. M. M. de Lima, M. Beck, R. Hey, *et al.*, "Compact Mach-Zehnder acousto-optic modulator," Appl. Phys. Lett. **89**(12), 121104 (2006).
11. E. S. K. Young, A. V. Akimov, M. Henini, *et al.*, "Subterahertz Acoustical Pumping of Electronic Charge in a Resonant Tunneling Device," Phys. Rev. Lett. **108**(22), 226601 (2012).
12. A. Dunn, C. Poyser, P. Dean, *et al.*, "High-speed modulation of a terahertz quantum cascade laser by coherent acoustic phonon pulses," Nat. Commun. **11**(1), 835 (2020).
13. A. Fainstein and B. Jusserand, "Raman scattering in resonant cavities," in *Light Scattering in Solid IX*, M. Cardona and R. Merlin, eds. (Springer Berlin Heidelberg, Berlin, Heidelberg, 2007), pp. 17–110.
14. A. Fainstein, N. D. Lanzillotti-Kimura, B. Jusserand, *et al.*, "Strong Optical-Mechanical Coupling in a Vertical GaAs/AlAs Microcavity for Subterahertz Phonons and Near-Infrared Light," Phys. Rev. Lett. **110**(3), 037403 (2013).
15. N. D. Lanzillotti-Kimura, A. Fainstein, B. Perrin, *et al.*, "Enhanced optical generation and detection of acoustic nanowaves in microcavities," Phys. Rev. B **83**(20), 201103 (2011).
16. O. Ortiz, F. Pastier, A. Rodriguez, *et al.*, "Fiber-integrated microcavities for efficient generation of coherent acoustic phonons," Appl. Phys. Lett. **117**(18), 183102 (2020).
17. O. Ortiz, P. Priya, A. Rodriguez, *et al.*, "Topological optical and phononic interface mode by simultaneous band inversion," Optica **8**(5), 598 (2021).
18. T. Czerniuk, D. Wigger, A. V. Akimov, *et al.*, "Picosecond Control of Quantum Dot Laser Emission by Coherent Phonons," Phys. Rev. Lett. **118**(13), 133901 (2017).
19. B. C. L. de Larrinzar, C. Xiang, E. R. C. de Oliveira, *et al.*, "Towards chiral acoustoplasmonics," Nanophotonics **12**(11), 1957–1964 (2023).
20. N. D. Lanzillotti-Kimura, K. P. O'Brien, J. Rho, *et al.*, "Polarization-controlled coherent phonon generation in acoustoplasmonic metasurfaces," Phys. Rev. B **97**(23), 235403 (2018).

Optical Materials EXPRESS

21. M. Poblet, R. Berté, H. D. Boggiano, *et al.*, "Acoustic Coupling between Plasmonic Nanoantennas: Detection and Directionality of Surface Acoustic Waves," ACS Photonics **8**(10), 2846–2852 (2021).
22. F. Della Picca, R. Berte, M. Rahmani, *et al.*, "Tailored Hypersound Generation in Single Plasmonic Nanoantennas," Nano Lett. **16**(2), 1428–1434 (2016).
23. D. L. Chafatinos, A. S. Kuznetsov, S. Anguiano, *et al.*, "Polariton-driven phonon laser," Nat. Commun. **11**(1), 4552 (2020).
24. A. S. Kuznetsov, D. H. O. Machado, K. Biermann, *et al.*, "Electrically Driven Microcavity Exciton-Polariton Optomechanics at 20 GHz," Phys. Rev. X **11**(2), 021020 (2021).
25. M. Kobecki, A. V. Scherbakov, S. M. Kukhtaruk, *et al.*, "Giant Photoelasticity of Polaritons for Detection of Coherent Phonons in a Superlattice with Quantum Sensitivity," Phys. Rev. Lett. **128**(15), 157401 (2022).
26. M. Esmann, F. R. Lamberti, A. Harouri, *et al.*, "Brillouin scattering in hybrid optophononic Bragg micropillar resonators at 300 GHz," Optica **6**(7), 854 (2019).
27. G. J. A. A. Soler-Illia and P. Innocenzi, "Mesoporous Hybrid Thin Films: The Physics and Chemistry Beneath," Chemistry: A European J. **12**, 4478–4494 (2006).
28. R. M. Gazoni, M. G. Bellino, M. Cecilia Fuertes, *et al.*, "Designed nanoparticle–mesoporous multilayer nanocomposites as tunable plasmonic–photonic architectures for electromagnetic field enhancement," J. Mater. Chem. C **5**(14), 3445–3455 (2017).
29. G. J. A. A. Soler-Illia, P. Vensaus, and D. Onna, "Chapter 6 - Chemical methods to produce mesoporous thin films with tunable properties," in *Chemical Solution Synthesis for Materials Design and Thin Film Device Applications*, S. Das and S. Dhara, eds. (Elsevier, 2021), pp. 195–229.
30. T. Hofmann, D. Wallacher, R. Toft-Petersen, *et al.*, "Phonons in mesoporous silicon: The influence of nanostructuring on the dispersion in the Debye regime," Microporous and Mesoporous Materials **243**, 263–270 (2017).
31. A. D. Pizarro, C. L. A. Berli, G. J. A. A. Soler-Illia, *et al.*, "Droplets in underlying chemical communication recreate cell interaction behaviors," Nat. Commun. **13**(1), 3047 (2022).
32. M. C. Fuertes, F. J. López-Alcaraz, M. C. Marchi, *et al.*, "Photonic Crystals from Ordered Mesoporous Thin-Film Functional Building Blocks," Adv. Funct. Mater. **17**, 1247–1254 (2007).
33. J. H. Pan, X. Zhao, and W. I. Lee, "Block copolymer-templated synthesis of highly organized mesoporous TiO2-based films and their photoelectrochemical applications," Chemical Engineering J. **170**(2-3), 363–380 (2011).
34. B. Auguié, M. C. Fuertes, P. C. Angelomé, *et al.*, "Tamm Plasmon Resonance in Mesoporous Multilayers: Toward a Sensing Application," ACS Photonics **1**(9), 775–780 (2014).
35. G. Benetti, M. Gandolfi, M. J. Van Bael, *et al.*, "Photoacoustic sensing of trapped fluids in nanoporous thin films: Device engineering and sensing scheme," ACS Appl. Mater. Interfaces **10**(33), 27947–27954 (2018). PMID: 30039696.
36. N. L. Abdala, M. Esmann, M. C. Fuertes, *et al.*, "Mesoporous thin films for acoustic devices in the gigahertz range," J. Phys. Chem. C **124**(31), 17165–17171 (2020).
37. E. R. Cardozo de Oliveira, C. Xiang, M. Esmann, *et al.*, "Probing gigahertz coherent acoustic phonons in TiO2 mesoporous thin films," Photoacoustics **30**, 100472 (2023).
38. C. Mechri, P. Ruello, and V. Gusev, "Confined coherent acoustic modes in a tubular nanoporous alumina film probed by picosecond acoustics methods," New J. Phys. **14**(2), 023048 (2012).
39. E. H. Hernando Abad, F. Bouyer, L. Chaabane, *et al.*, "Sub-THz Vibrational Dynamics in Ordered Mesoporous Silica Nanoparticles," Nanomaterials **13**(14), 2078 (2023).
40. N. Hidalgo, M. E. Calvo, M. G. Bellino, *et al.*, "Porous Supramolecularly Templated Optical Resonators Built in 1D Photonic Crystals," Adv. Funct. Mater. **21**, 2534–2540 (2011).
41. M. E. Calvo, N. Hidalgo, R. Schierholz, *et al.*, "Full solution processed mesostructured optical resonators integrating colloidal semiconductor quantum dots," Nanoscale **7**(40), 16583–16589 (2015).
42. C. Thomsen, J. Strait, Z. Vardeny, *et al.*, "Coherent Phonon Generation and Detection by Picosecond Light Pulses," Phys. Rev. Lett. **53**(10), 989–992 (1984).
43. P. Ruello and V. E. Gusev, "Physical mechanisms of coherent acoustic phonons generation by ultrafast laser action," Ultrasonics **56**, 21–35 (2015).
44. N. D. Lanzillotti-Kimura, A. Fainstein, B. Perrin, *et al.*, "Theory of coherent generation and detection of THz acoustic phonons using optical microcavities," Phys. Rev. B **84**(6), 064307 (2011).
45. O. Matsuda and O. B. Wright, "Reflection and transmission of light in multilayers perturbed by picosecond strain pulse propagation," J. Opt. Soc. Am. B **19**(12), 3028 (2002).
46. B. Perrin, C. Rossignol, B. Bonello, *et al.*, "Interferometric detection in picosecond ultrasonics," Physica B: Condensed Matter **263-264**, 571–573 (1999).
47. T. H. Fung, T. Veeken, D. Payne, *et al.*, "Application and validity of the effective medium approximation to the optical properties of nano-textured silicon coated with a dielectric layer," Opt. Express **27**(26), 38645 (2019).
48. A. M. Ruminski, M. M. Moore, and M. J. Sailor, "Humidity-Compensating Sensor for Volatile Organic Compounds Using Stacked Porous Silicon Photonic Crystals," Adv. Funct. Mater. **18**, 3418–3426 (2008).
49. M. C. Sansierra, J. Morrone, F. Cornacchiulo, *et al.*, "Detection of Organic Vapors Using Tamm Mode Based Devices Built from Mesoporous Oxide Thin Films," ChemNanoMat **5**, 1289–1295 (2019).
50. C. Colvard, T. A. Gant, M. V. Klein, *et al.*, "Folded acoustic and quantized optic phonons in (gaal)as superlattices," Phys. Rev. B **31**(4), 2080–2091 (1985).

Optical Materials EXPRESS

51. V. Narayanamurti, H. L. Störmer, M. A. Chin, *et al.*, "Selective transmission of high-frequency phonons by a superlattice: The dielectric phonon filter," Phys. Rev. Lett. **43**(27), 2012–2016 (1979).
52. J. V. Jäger, A. V. Scherbakov, B. A. Glavin, *et al.*, "Resonant driving of magnetization precession in a ferromagnetic layer by coherent monochromatic phonons," Phys. Rev. B **92**(2), 020404 (2015).
53. C.-K. Sun, J.-C. Liang, and X.-Y. Yu, "Coherent acoustic phonon oscillations in semiconductor multiple quantum wells with piezoelectric fields," Phys. Rev. Lett. **84**(1), 179–182 (2000).
54. G. N. Aliev, B. Goller, D. Kovalev, *et al.*, "Hypersonic acoustic mirrors and microcavities in porous silicon," Appl. Phys. Lett. **96**(12), 124101 (2010).
55. A. Crespo-Poveda, A. S. Kuznetsov, A. Hernández-Mínguez, *et al.*, "GHz guided optomechanics in planar semiconductor microcavities," Optica **9**(2), 160 (2022).
56. N. D. Lanzillotti-Kimura, A. Fainstein, B. Perrin, *et al.*, "Enhancement and Inhibition of Coherent Phonon Emission of a Ni Film in a BaTiO 3 / SrTiO 3 Cavity," Phys. Rev. Lett. **104**(18), 187402 (2010).
57. C. Boissiere, D. Grosso, S. Lepoutre, *et al.*, "Porosity and Mechanical Properties of Mesoporous Thin Films Assessed by Environmental Ellipsometric Porosimetry," Langmuir **21**(26), 12362–12371 (2005).
58. M. I. Velasco, M. B. Franzoni, E. A. Franceschini, *et al.*, "Water confined in mesoporous tio2 aerosols: Insights from nmr experiments and molecular dynamics simulations," J. Phys. Chem. C **121**(13), 7533–7541 (2017).
59. E. González Solveyra, E. de la Llave, V. Molinero, *et al.*, "Structure, dynamics, and phase behavior of water in tio2 nanopores," J. Phys. Chem. C **117**(7), 3330–3342 (2013).
60. G. Y. Gor, L. Bertinetti, N. Bernstein, *et al.*, "Elastic response of mesoporous silicon to capillary pressures in the pores," Appl. Phys. Lett. **106**(26), 261901 (2015).
61. G. Giménez, G. Ybarra, and G. J. A. A. Soler-Illia, "Preparation of mesoporous silica thin films at low temperature: A comparison of mild structure consolidation and template extraction procedures," J. Sol-Gel Sci. Technol. **96**(2), 287–296 (2020).
62. D. H. Machado, A. Crespo-Poveda, A. S. Kuznetsov, *et al.*, "Generation and Propagation of Superhigh-Frequency Bulk Acoustic Waves in Ga As," Phys. Rev. Appl. **12**(4), 044013 (2019).